Energy & Environmental Science

Investigations of the Stability of Etched or Platinized p-InP(100) Photocathodes for Solar-driven Hydrogen Evolution in Acidic or Alkaline Aqueous Electrolytes

Journal:	*Energy & Environmental Science*
Manuscript ID	EE-ART-09-2021-002809.R1
Article Type:	Paper
Date Submitted by the Author:	22-Sep-2021
Complete List of Authors:	Yu, Weilai; California Institute of Technology, Division of Chemistry and Chemical Engineering Richter, Matthias; California Institute of Technology, Joint Center for Artificial Photosynthesis Buabthong, Pakpoom; California Institute of Technology, Division of Engineering and Applied Science, Joint Center for Artificial Photosynthesis Moreno-Hernandez, Ivan; California Institute of Technology, Chemistry and Chemical Engineering Read, Carlos; California Institute of Technology, Division of Chemistry and Chemical Engineering Simonoff, Ethan; California Institute of Technology, Chemistry Brunschwig, Bruce; California Institute of Technology , Beckman Institute Lewis, Nathan S.; California Institute of Technology, Chemistry and Chemical Engineering

Investigations of the Stability of Etched or Platinized p-InP(100) Photocathodes for Solar-driven Hydrogen Evolution in Acidic or Alkaline Aqueous Electrolytes

Weilai Yu[1], Matthias H. Richter[1,2], Pakpoom Buabthong[2], Ivan A. Moreno-Hernandez[1], Carlos G. Read[1], Ethan Simonoff[1], Bruce S. Brunschwig[3] and Nathan S. Lewis[1,3*]

[1]Division of Chemistry and Chemical Engineering, [2]Division of Engineering and Applied Science, and [3]Beckman Institute Molecular Materials Resource Center (MMRC), California Institute of Technology, Pasadena CA, 91125

Email: nslewis@caltech.edu

Abstract

The stability of p-InP photocathodes performing the hydrogen-evolution reaction (HER) has been evaluated in contact with either 1.0 M H_2SO_4(aq) or 1.0 M KOH(aq), with a focus on identifying corrosion mechanisms. Stability for the solar-driven HER was evaluated using p-InP electrodes that were either etched or coated with an electrodeposited Pt catalyst (p-InP/Pt). Variables such as trace O_2 were systematically controlled during the measurements. Changes in surface characteristics after exposure to electrochemical conditions as well as electrode dissolution processes were monitored using X-ray photoelectron spectroscopy (XPS) and inductively coupled plasma mass spectrometry (ICP-MS).

In either H_2SO_4 or KOH, etched p-InP photoelectrodes corroded cathodically under illumination, forming metallic In^0 at the electrode surface. In contrast, electrodeposition of Pt kinetically stabilized illuminated p-InP photocathodes in both H_2SO_4 and KOH by inhibiting the cathodic corrosion pathway. Notably, when held at 0 V vs the reversible hydrogen electrode (RHE) in 1.0 M H_2SO_4(aq), p-InP/Pt exhibited a stable current density (J) of ~-18 mA cm^{-2} for >285 h under simulated 1-sun illumination. The long-term current density vs potential (J-E) behavior at pH 0 and pH 14 of p-InP/Pt photocathodes correlated with changes in the surface chemistry as well as the dissolution of p-InP. In acidic media, the J-E behavior of p-InP/Pt photocathodes remained nearly constant with time, but the surface of p-InP/Pt electrodes gradually turned P-rich via a slow and continuous leaching of In ions. In alkaline electrolyte, the surface of p-InP/Pt electrodes was passivated by formation of an InO_x layer that exhibited negligible dissolution but led to a substantial degradation in the J-E characteristics. Consequently, changes in the catalytic kinetics and surface stoichiometry are both important considerations for determining the corrosion chemistry and the long-term operational stability of InP photoelectrodes.

Introduction

Stability is the most persistent materials challenge limiting the development of operational, efficient integrated solar-driven water-splitting cells. Although a solar-to-hydrogen energy-conversion efficiency $\eta_{STH} \geq 10\%$ was reported over twenty years ago,[1] and cell efficiencies have improved gradually to $\geq 15\%$,[2–6] such efficiencies are rarely, if ever, maintained for more than a few days in the laboratory.

Maximizing the theoretically achievable efficiency of a water-splitting cell requires the use of a highly acidic or highly alkaline electrolytes, to limit pH gradients in the cell and to provide high ionic conductivities without a loss of energy associated with electrodialysis of the electrolyte buffer species.[7,8] However, the aggressive electrochemical environment required for maximum operational efficiency presents challenges to the stability of the materials in the device. For example, known semiconductors with band gaps ($\mathbf{E}_g$) useful for absorbing a substantial portion of the solar spectrum ($\mathbf{E}_g \leq 2.2$ eV)[9] are thermodynamically unstable when operated as photoanodes at potentials needed to effect the water-oxidation half-reaction in strongly acidic or alkaline aqueous electrolytes.[10–14] In contrast, thermodynamic calculations suggest that many semiconductors, including GaP, InP, GaAs, and Si, are predicted to be electrochemically stable when used as hydrogen-evolving cathodes in aqueous electrolytes.[11]

Group III-V semiconductors, such as InP, GaP, and GaAs, are attractive candidates for use in efficient tandem solar-driven water-splitting cells, because high-efficiency multijunction photovoltaic cells can be made using epitaxial growth and lift-off techniques.[15] Alloying within the Group III-V materials allows band-gap tuning of the light absorbers to optimize their properties for a solar-driven water-splitting cell.[16] Furthermore, the conduction-band edges of III-V materials are located favorably relative to the water-reduction potential. Group III-V materials have been the foundation of nearly all solar water-splitting cells that have exhibited $\eta_{STH} \geq 10\%$.[1,3,5,6,17]

P-type InP (p-InP) has been studied as a photocathode in hydrogen-evolving cells with acidic electrolytes, including water-splitting and hydrohalic acid-splitting cells, but has rarely been examined as a photocathode in hydrogen-evolving cells with alkaline electrolytes.[18–24] Differential

electrochemical mass spectrometry (DEMS) of illuminated etched p-InP(111) photocathodes in contact with 0.5 M H_2SO_4(aq) has revealed a photocorrosion process involving evolution of PH_3(g).[25] A more recent study using on-line electrochemical mass spectrometry (OLEMS) has shown that PH_3 evolution accompanies hydrogen evolution on illuminated etched p-InP(100) photocathodes.[26] p-InP has been reported to act as a stable photocathode for the reduction of VCl_3 to VCl_2 in HCl.[20,27] However with hydrogen-evolution reaction (HER) catalysts of metallic Ru, Rh, or Pt, p-InP photocathodes displayed stable photocurrents in 1 M HCl (in the absence of O_2) only when the electrode was electrically disconnected every 20 min.[18,28] Electrodeposition of Pt onto the p-InP surface was found to also suppress the cathodic photocorrosion by accelerating the kinetics of the HER.[25]

Typically, experimental investigations of photoelectrode stability are not conducted for more than a few hours, and do not measure the electrode dissolution with sensitivity levels sufficient to detect the corrosion of 1 nm of the electrode. For evaluation of multi-year use in solar-driven water-splitting devices, the long-term dissolution rate of semiconductors needs to be defined quantitatively, in conjunction with a detailed assessment of the changes in the electrode surface as a result of sustained photoelectrode operation. Combined with the thermodynamic Pourbiax diagram, such experimental studies can provide a comprehensive understanding of the corrosion mechanism and form a basis for systematically improving the durability of such systems.

Theoretical predictions of thermodynamic materials stability generally do not consider reactions involving O_2. Additional corrosion pathways may result from the sensitivity of III-V materials to O_2, such as dissolution induced by surface oxidation.[18] Phenomenological investigations of electrode stability generally do not rigorously control the concentration of dissolved O_2 in the catholyte. Possible oxidation of the electrode surface by ambient O_2(g) after electrochemical measurements may further convolute the analysis of a pristine electrode surface. Based on these considerations, a comparison between theoretical expectations and experimental observations would benefit from careful control over possible reactions between the electrode surface and O_2.

Herein we systematically evaluate the stability of InP for use as a photocathode for the HER in both 1.0 M H_2SO_4(aq) or 1.0 M KOH(aq). We focus on establishing both the mechanisms and rates

of corrosion reactions observed under hydrogen-evolving conditions. Electrochemical experiments and X-ray photoelectron spectroscopic (XPS) measurements were performed without exposing the electrodes to O_2, and were performed for etched p-InP and n-InP, as well as for p-InP with an electrodeposited Pt catalyst. The surface conditions of the InP electrodes were compared by XPS analysis before and after exposure to electrochemical conditions. Quantitative analyses by ICP-MS of electrode dissolution into the electrolyte were performed throughout the electrochemical experiments. Considering the thermodynamic Pourbaix diagram, the corrosion pathways of p-InP were determined at both pH 0 and pH 14, with and without a Pt catalyst on the electrode surface. The long-term evolution of the *J-E* behavior of these photoelectrodes was monitored during the stability tests. Consequently, the changes in photoelectrochemical (PEC) performance were correlated with dissolution as well as with changes in the composition and morphology of the semiconductor photoelectrode surfaces.

Methods

More detailed experimental descriptions are provided in the Supplementary Information.

Electrode preparation: Single-side polished, (100)-oriented, Sn-doped (N_d = 1-5×10^{17} cm^{-3}), n-type InP wafers and Zn-doped (N_d = 1-5×10^{17} cm^{-3}), p-type InP wafers were purchased from AXT Inc. Ohmic back contacts to n-type InP were made by sputtering 20 nm of Ni onto the back (unpolished) side of the n-InP wafer, followed by annealing under forming gas at 400 °C for 10 min. Ohmic back contacts to p-type InP were made by sputtering 10 nm of Zn and then 90 nm of Au onto the back side of the wafer, followed by annealing under forming gas at 400 °C for 10 min.

Prior to electrochemical measurements, all InP samples were first etched in a solution of 0.04 % (by volume) Br_2/CH_3OH for 30 s, then in 4.0 M NH_3/CH_3OH for 30 s followed by rinsing in pure CH_3OH for 10 s. The etching and rinsing cycle was then repeated two more times, whereas electrodes were finally blown dry by N_2(g) for >10 s.

Electrolyte purification: Before use in stability tests, the 1.0 M H_2SO_4(aq) and 1.0 M KOH(aq) electrolytes were first pre-electrolyzed in a two-compartment electrochemical cell with either a Nafion (acid) or Fumasep (base) membrane. For pre-electrolysis, either a constant bias of > 3 V or a constant current of 6 mA for > 24 h, was applied to two separate carbon cloth or carbon rod electrodes. Only the pre-electrolyzed electrolyte in the cathode compartment was then collected and used in the following electrochemical measurements.

Stability tests: (Photo)-electrochemical measurements of InP samples that required further XPS analysis were performed in a N_2-filled glovebox (VAC, OMNI-LAB). All electrolytes were first degassed using a Schlenk line, and transferred and stored in the glovebox. Electrochemical data were collected on a SP-200 potentiostat (BioLogic Science Instruments) without compensating the series resistance of the solution. To facilitate XPS analysis, electrochemical measurements were performed using a custom electrochemical compression cell fabricated from PEEK, in a three-electrode set-up (Figure S1). A leakless miniature AgCl/Ag electrode (eDAQ, ET072-1) or a hydrogen electrode HydroFlex (Gaskatel) was used as the reference electrode. A Pt foil (for H_2SO_4) or a Ni foil (for KOH) was used as the counter electrode. During (Photo)-electrochemical experiments, H_2(g) was fed into the glovebox to constantly purge the catholyte after passing through a gas bubbler (Figure S2a-b). Separate gas outlets were provided for the cathode chamber (H_2) and the anode chamber (O_2). Besides, light illumination was introduced from the illumination source into the glove box via the fiber optic. A miniature fiber-optic adjustable-arm light equipped with a 150 W halogen bulb was used as the illumination source. The illumination intensity at the sample location in the cell was calibrated to 1 Sun (100 mW cm^{-2}) using a Si photodiode (FDS100, Thorlabs).

Prior to each experiment, the electrochemical cell was assembled immediately after InP etching, and the assembled cell was then promptly transferred into the glovebox. During electrochemical experiment, 0.2 mL of electrolyte was removed from the cathode chamber for IC-MS analysis at different time intervals, whereas the electrode was still under potential control. Then 0.2 mL of fresh electrolyte was added to keep the total volume (3-4 mL) constant. Upon completion of each experiment, the electrochemical cell was first disassembled inside the glove box. The electrode

sample was thoroughly rinsed with deionized water, dried under stream of flowing N_2(g), and stored inside the glove box until further XPS analysis.

To periodically measure the *J-E* behavior of photoelectrodes, chronoamperometry (CA) was first interrupted by a short period (15 s) of open circuit while measuring E_{oc}, followed by three cycles of consecutive cyclic voltammetry (CV). CV was started from $E_{start} = E_{oc}$-30 mV to < 0 V vs RHE and then ended at $E_{end} = E_{oc}$-80 mV in the return scan, to avoid passing anodic current through the InP electrodes.

Electrodeposition of Pt: Electrodeposition of Pt particles on InP was carried out in an aqueous solution of 5 mM K_4PtCl_6 and 0.5 M KCl in a two-electrode configuration. A constant current density of -0.2 mA cm^{-2} was applied to the InP working electrode until a fixed charge of 20 mC cm^{-2} had passed, whereas a Pt wire or a carbon rod was used as the counter electrode. The electrodeposition was performed under ~1 sun illumination for p-InP and in the dark for n-InP.

Electrochemistry outside the glovebox: To evaluate the stripping behavior of plated In^0 metals on InP, a series of CA followed by CV experiments were performed for n-InP (dark) and p-InP (1-sun illumination) electrodes. A two-compartment cell was used outside the glove box under a continuous H_2 purge (Figure S2d). The CA-CV experiments started by potentiostatically holding freshly etched InP electrodes at specified potentials for 30 min. Then at least three CVs were scanned from the original applied potential to sufficiently positive potentials to oxidize any plated In^0 metal. Epoxy-encapsulated InP electrodes were used as the working electrodes. A $Hg/HgSO_4$ in saturated K_2SO_4(aq) and a Hg/HgO in 1.0 M KOH (aq) reference electrodes were used for measurements in 1.0 M H_2SO_4(aq) and 1.0 M KOH (aq), respectively. A carbon rod placed within a fritted glass tube was used as the counter electrode. To determine the interfacial energetics, impedance measurements of freshly etched n-InP and p-InP electrodes were performed with the same three-electrode setup in the dark, in contact with 1.0 M H_2SO_4(aq) or 1.0 M KOH(aq) under H_2(g) bubbling. A frequency range of 20 Hz to 20 kHz was used with a sinusoidal wave amplitude of 25 mV.

Analytical methods: To determine the concentrations of dissolved In ions in electrolyte, inductively coupled plasma mass spectrometry (ICP-MS) data were collected using an Agilent 8800 Triple

Quadrupole ICP-MS system. All electrolyte samples were diluted and acidified to pH ≤2 before the measurements. The total amounts of In ions in the electrolyte were calculated and normalized to the geometric electrode area to yield the equivalent corrosion thicknesses (nm) of the InP electrode.

X-ray photoelectron spectroscopy (XPS) data was collected using a Kratos Axis Ultra system with a base pressure of < 1×10^{-9} Torr, equipped with a monochromatic Al Kα X-ray source with a photon energy of 1486.6 eV. Prior to XPS measurements, samples were mounted on a sample holder and loaded in a transfer box inside the N_2-filled glovebox. Samples were then transferred from the glovebox to the XPS without any exposure to air (Figure S2c).

Scanning-electron microscopy (SEM) images were obtained on a Nova NanoSEM 450 (FEI) with an accelerating voltage of 5 kV. Transmission-electron microscopy (TEM) cross-sections of the samples were prepared using a focused Ga ion beam (FIB), on a FEI Nova-600 Nanolab FIB/FESEM or a FEI Helios NanoLab G4 Dual Beam. TEM images of the prepared lamella samples were obtained using a Tecnai Polara (F30) TEM at an accelerating voltage of 300 kV, or a FEI Osiris at an accelerating voltage of 200 kV equipped with a Gatan 2K TEM camera and Bruker EDS. Atomic-force microscopy (AFM) images were obtained on a Bruker Dimension Icon using Bruker ScanAsyst-Air probes operating in the ScanAsyst mode.

Results

A. Stability of illuminated etched p-InP electrodes during the HER.

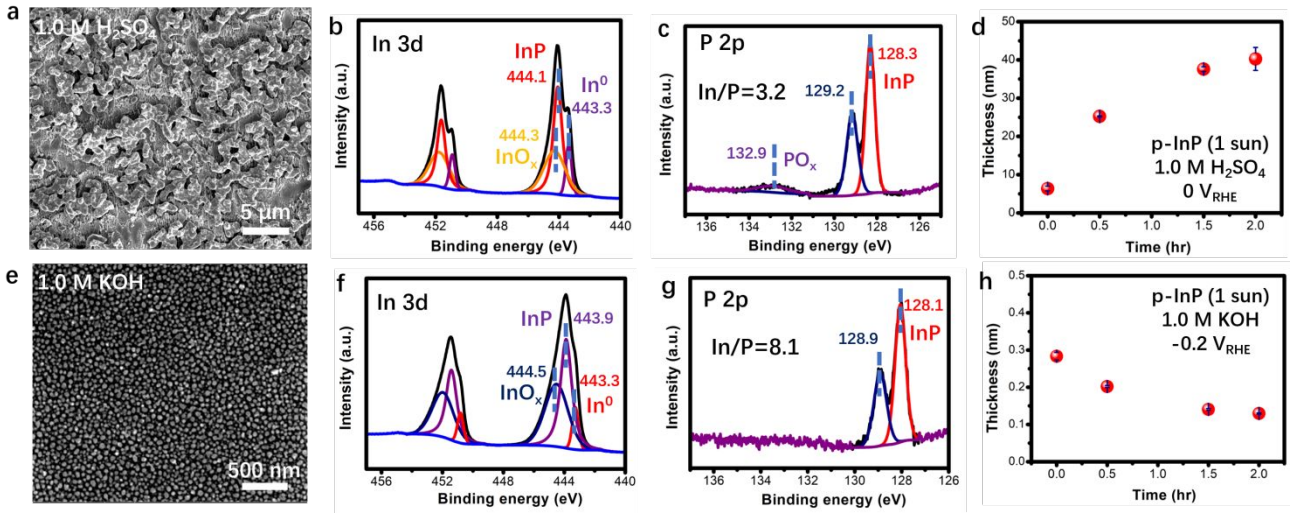

Figure 1. Surface analyses of illuminated etched p-InP electrodes (1-sun) after 2 h of chronoamperometry (CA) at (a-d) E = 0 V vs the reversible hydrogen electrode (RHE) in contact with 1.0 M H_2SO_4(aq), and (e-h) E = -0.2 V vs RHE in contact with 1.0 M KOH(aq). (a,e) SEM images showing the morphology of electrode surfaces. (b,c,f,g) XPS data of the (b,f) In 3d and (c,g) P 2p regions after the 2 h CA. (d,h) Total amount of dissolved In ions in the electrolyte during the 2 h CA, calculated as the equivalent depth of InP dissolved from the electrode surface.

Figure 1 presents surface analyses after 2-h of chronoamperometry (CA) to assess the cathodic stability of illuminated (1 sun) etched p-InP electrodes in contact with either 1.0 M H_2SO_4(aq) or 1.0 M KOH(aq). During CA at E = 0 V vs. the reversible hydrogen electrode (RHE) in 1.0 M H_2SO_4(aq), within the first 20 min the current density ($|J|$) of an illuminated etched p-InP electrode decreased from ~9 mA cm^{-2} to 1 mA cm^{-2} (Figure S3). After 2 h, the electrode surface was covered by a white film, and the SEM image showed a fibrous morphology on the surface (Figure 1a). XPS analysis of the In $3d_{5/2}$ spectral region revealed a large peak for the In^{3+} cations of InP (binding energy, BE=444.1 eV), accompanied by a peak at lower binding energy, BE = 443.3 eV, ascribable to metallic In^0 (Figure 1b). The P 2p XPS data showed the P^{3-} anions of InP (BE=128.3/129.2 eV) with minimal surface phosphates (BE≈133 eV) (Figure 1c). Before CA, a fresh p-InP sample displayed an In/P atomic ratio of 1.3 at the surface (Figure S4), whereas after the CA in H_2SO_4, the In/P atomic

ratio increased to 3.2, indicating enrichment of In at the surface. The concentration of dissolved In ions in the acidic electrolyte increased over the 2 h experiment, implying dissolution of >40 nm in depth of InP (Figure 1d).

During CA at E = -0.2 V vs RHE in 1.0 M KOH(aq), in the first 10 min, the $|J|$ of an illuminated etched p-InP decreased from ~6 mA cm^{-2} to 0.5 mA cm^{-2} (Figure S5). After the 2-h CA, the surface of the p-InP electrode was covered uniformly by densely packed nanoparticles (Figure 1e). After the CA of p-InP at -0.2 V vs RHE in 1.0 M KOH(aq), a peak at BE = 443.3 eV, corresponding to metallic In^0, was observed in the In 3d XPS region (Figure 1f), similar to the results in acid described above. The peak at higher BE = 444.5 eV is attributable to the presence of surface oxide (InO_x), consistent with the peak in the O 1s XPS region at BE = 529.6 eV (Figure S6).[29] The P 2p XPS region only showed peaks ascribable to P^{3-} anions in InP, whereas after the CA the 8.1:1 In/P ratio indicated a substantial enrichment of In relative to P (Figure 1g). However, the concentration of dissolved In ions in the alkaline electrolyte was negligible and did not increase with time (Figure 1h).

Collectively, these results clearly show the formation of metallic In^0 on the surface of illuminated etched p-InP electrodes under cathodic conditions in both 1.0 M H_2SO_4(aq) and 1.0 M KOH(aq).

The stripping behavior of plated In^0 metal on the surfaces of n-InP electrodes was explored in the dark and on p-InP under 1-sun illumination, at both pH 0 and pH 14. A series of 30-min CAs were performed for n-InP electrodes in the dark and for p-InP electrodes under illumination as a function of the electrode potential, E, followed by CV scans from the originally applied E towards more positive E values. The CA initiated the cathodic corrosion of InP to In^0 metal, whereas the CV was used to observe the onset potential of In^0 oxidation on the InP surface.

Initially, a series of CAs at E between -0.4 to -0.9 V vs RHE was performed for n-InP electrodes in the dark (Figure 2a-b and Figure S7). Figure 2a-b shows the first CV sweeps of the electrodes after CA in 1.0 M H_2SO_4(aq) and KOH(aq), respectively. In 1.0 M H_2SO_4(aq), an anodic wave with an onset E (E_{on}) of ~ -0.4 V vs RHE was observed during the first CV sweep for n-InP electrodes that had been initially held at $E \leq$ -0.6 V vs RHE (Figure 2a and Figure S7). The value of J during the

anodic wave increased as the electrodes were held at increasingly negative potentials during the CA. Typically, the anodic waves disappeared after the second CV cycle (Figure S8). For comparison, E_{on} of anodic current for an In metal foil electrode in 1.0 M H_2SO_4(aq) was ~-0.36 V vs RHE (Figure S9). The observed anodic waves of n-InP electrodes held at $E \leq$-0.6 V vs RHE in the dark thus correspond to the stripping of In^0 metal plated onto the InP surface during the prior 30 min CAs (Eq 1):

$$In \rightleftarrows In^{3+} + 3e^- \qquad E^0 = -0.342 + 0.0197 \log [In^{3+}] \text{ V vs. NHE} \qquad (1)$$

Thus, the disappearance of anodic waves after the second CV cycle in Figure S8 suggests complete removal of plated In^0 metal from electrode surface in acidic electrolyte.

In 1.0 M KOH(aq), two anodic waves, one with E_{on}~-0.2 V vs RHE and the other with E_{on}~-0.1 V vs RHE were observed during the positive scan of the first CV for n-InP electrodes that had been held at $E \leq$ -0.4 V vs RHE (Figure 2b and Figure S7). A single reductive peak was observed at $E \sim$ -0.25 V vs RHE in the return scan. Similar to the behavior in acid, electrodes that had been initially held at more negative potentials exhibited larger peaks in J. However, the redox waves of InP electrodes remained after consecutive CV cycling, indicating that the plated In^0 did not rapidly dissolve (Figure S10). Similarly positioned anodic and cathodic waves were observed in the CVs of an In metal foil electrode in 1.0 M KOH(aq) (Figure S11). The peak J depended linearly on scan rate, consistent with a redox process confined to a single monolayer of In atoms (Figure S9b). Thus, the anodic waves observed after the CAs are consistent with the oxidation of metallic In^0 plated on the electrode surface to anhydrous and hydrated In(III) oxide (Eq 2a-b):[10,30]

$$In + 3OH^- \rightleftarrows In(OH)_3 + 3e^- \qquad E^0 = -0.172 \text{ V versus RHE} \qquad (2a)^{10}$$

$$2In + 6OH^- \rightleftarrows In_2O_3 + 3H_2O + 6e^- \qquad E^0 = -0.190 \text{ V versus RHE} \qquad (2b)^{10}$$

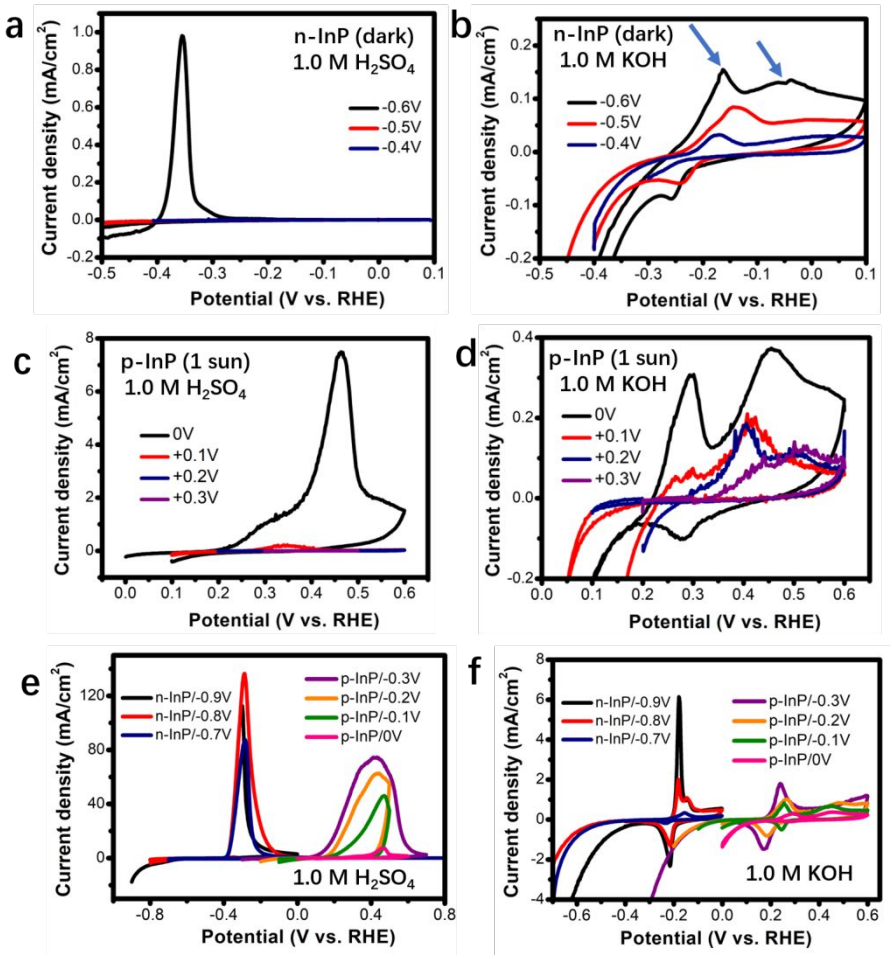

Figure 2. (a-b) Comparison of the 1st CV obtained after the 30-min CAs of n-InP electrodes at *E* from -0.6 to -0.4 V vs RHE in the dark in (a) 1.0 M H_2SO_4(aq) and (b) 1.0 M KOH(aq); (c-d) Comparison of the first CV obtained after the 30-min CAs of p-InP electrodes under 1-sun illumination at *E* from 0 to 0.3 V vs RHE in (c) 1.0 M H_2SO_4(aq) or (d) 1.0 M KOH(aq). (e-f) Comparison of the CVs of n-InP dark electrodes and illuminated p-InP electrodes, respectively, after 30-min CAs at different potentials, in (e) 1.0 M H_2SO_4(aq) and (f) 1.0 M KOH(aq). All CVs were scanned in positive direction from the initially applied E (scan rate: 20 mV s^{-1}).

In parallel, a series of 30-min CAs was performed for p-InP electrodes under 1-sun illumination between E = 0.3 and -0.3 V vs RHE, in both 1.0 M H_2SO_4(aq) and 1.0 M KOH(aq) (Figure 2c-d and Figure S12). In the post-CA CVs, anodic waves similar to those exhibited by n-InP were observed in both electrolytes. However, the potentials of the waves were offset positively for the p-InP electrodes held at $E \leq$ +0.2 V vs RHE in 1.0 M H_2SO_4(aq), and for all p-InP electrodes tested in 1.0 M KOH(aq). p-InP electrodes that had been held at negative *E* exhibited large peaks in *J*. These anodic

waves are consistent with the deposition of metallic In^0 on the surface of illuminated p-InP electrodes during the prior 30-min CAs.[31,32] As shown in Figure 2e-f, comparisons between In^0 stripping waves in the CVs reveals positive shifts from n-InP (dark) to p-InP (light) by >550 mV and >400 mV in 1.0 M H_2SO_4(aq) and 1.0 M KOH(aq), respectively.

B. Stability of illuminated p-InP/Pt electrodes during the HER.

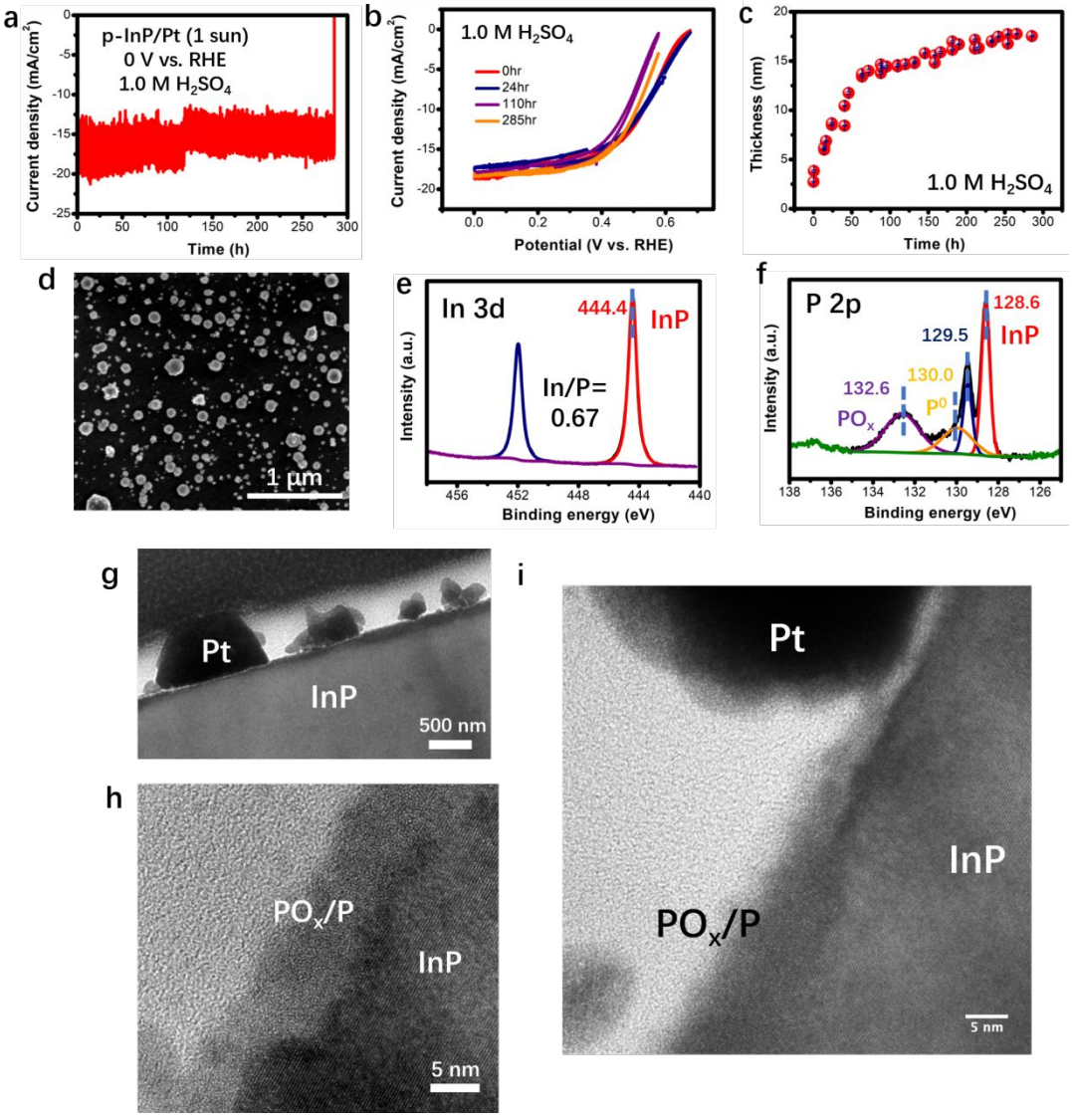

Figure 3. (a) CA of a p-InP/Pt photoelectrode at 0 V vs RHE in 1.0 M H_2SO_4(aq) under 1-sun illumination. (b) Comparison of *J-E* behaviors of a p-InP/Pt electrode (scan rate: 50 mV s^{-1}) and (c) the corrosion thickness of InP over time measured during the CA in (a). (d) SEM image and (e-f) XP

spectra in the (e) In 3d and (f) P 2p regions, and (g-i) cross-sectional TEM images of the p-InP/Pt electrode after the 285 h of CA in (a).

The behavior of etched InP electrodes was also compared to the behavior of InP electrodes that had a layer of Pt catalyst electrodeposited onto the surface. Pt was electrodeposited over the surface of an illuminated p-InP electrode (1 sun) at J = -0.2 mA cm^{-2} in a Pt plating solution, and the resulting p-InP/Pt electrodes were subsequently evaluated by CA at 0 V vs RHE in either 1.0 M H_2SO_4(aq) or 1.0 M KOH(aq). The SEM image showed that the electrodeposited Pt was present as sparsely distributed particles on the electrode surface (Figure S13). XPS analysis of the as-prepared p-InP/Pt electrode revealed a nearly stoichiometric InP surface (In/P=1.1) with minimal PO_x (Figure S14).

Prior to CA, the p-InP/Pt electrode yielded an open-circuit potential (E_{oc}) of 0.71±0.01 V vs RHE in contact with 1.0 M H_2SO_4(aq) under simulated 1-sun illumination (Figure S15). During the CA at E = 0 V vs RHE in 1.0 M H_2SO_4(aq), the illuminated p-InP/Pt electrode exhibited a stable $|J|$ of 17.9±1.4 mA cm^{-2} for >285 h (Figure 3a). A gradual decrease of E_{oc} to ~0.55 V vs RHE was observed in the first 150 h and then towards the end of the experiment E_{oc} slightly increased to ~0.62 V vs RHE (Figure S15). Despite the slight changes in E_{oc}, periodic measurements revealed essentially no change in the J-E behavior of p-InP/Pt electrodes during the CA (Figure 3b). Within the first 50 h of the CA, the leaching rate of In ions from p-InP into the electrolyte was ~0.15 nm h^{-1}, and after 150 h the leaching rate decreased to 0.03 nm h^{-1} (Figure 3c). After the 285 h CA, SEM images showed that the electrodeposited Pt particles remained on the surface (Figure 3d).

After the CA, the XPS data in the In 3d region only showed a single peak ascribed to the In^{3+} cations of InP, with no observed peak attributable to metallic In^0 (Figure 3e). The XPS data in the P 2p region revealed a pronounced peak at 132.7 eV, attributable to oxidized phosphorous (PO_x) at the electrode surface (Figure 3f). A new peak attributable to elemental P^0 emerged at BE =130.0 eV. The In/P atomic ratio decreased to ~0.67, indicating an enrichment of P over In at the electrode surface.

Consistent with the SEM image of p-InP/Pt after the CA, electrodeposited Pt was visible as discrete nm-sized particles in the cross-sectional TEM image of the p-InP substrate (Figure 3g).

Close examination of the p-InP surface revealed an amorphous overlayer with a maximum thickness of 8 nm on the regions of p-InP that were not covered by Pt particles. This layer is attributable to the oxidized phosphorous and elemental P^0 species observed in the XPS data (Figure 3h-i). In contrast, the amorphous layer was much thinner (~2 nm) in the regions directly beneath the Pt particles.

To better understand the formation of a P-rich surface of p-InP/Pt after the long-term CA, two other p-InP/Pt electrodes were evaluated at E = 0 V vs RHE under simulated 1-sun illumination, for 1 h and for 25 h, respectively, without intermediate *J-E* scans. XPS analyses indicated that the surfaces of both electrodes remained nearly stoichiometric (In/P=1.2) with minimal oxidized phosphorus (Figure S16). These results suggest that the observed P-enrichment of the electrode surface developed over longer term (>25 h) of the CA.

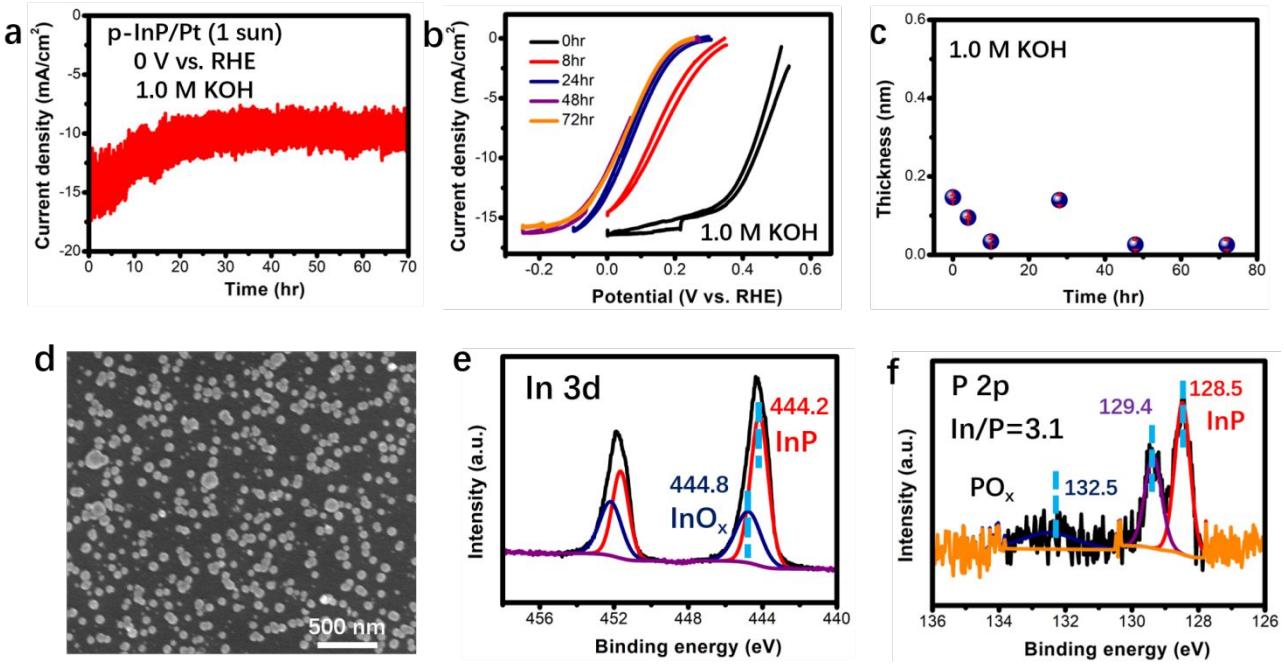

Figure 4. (a) CA for a p-InP/Pt electrode held at 0 V vs RHE in 1.0 M KOH(aq) under 1-sun illumination. (b) Comparison of the *J-E* behavior of a p-InP/Pt electrode (scan rate: 50 mV s^{-1}) and (c) the corrosion thickness of InP over time measured during the test in (a). (d) SEM image of p-InP/Pt electrode surface after 72 h of operation. (e-f) XP spectra of the (e) In 3d and (f) P 2p regions of a p-InP/Pt electrode after 72 h of operation in (a).

In 1.0 M KOH(aq), the initial E_{oc} of the illuminated (simulated 1 sun) p-InP/Pt electrode was 0.63±0.03 V vs RHE, ~80 mV lower than the initial E_{oc} measured in 1.0 M H_2SO(aq). Within the

first 24 h at E = 0 V vs RHE under simulated 1-sun illumination, $|J|$ for the p-InP/Pt electrode in 1.0 M KOH(aq) gradually decreased from ~17 mA cm^{-2} to ~12 mA cm^{-2}, and subsequently remained nearly unchanged (Figure 4a). The decrease in $|J|$ is attributable to a substantial shift of the *J-E* behavior towards negative potentials during the first 24 h of the CA (Figure 4b). In contrast, the *J-E* behavior of the p-InP/Pt electrode remained nearly unchanged between 24 and 72 h of operation. Notably, the light-limited current density (J_{ph}) in the measured *J-E* behavior remained at ~ -17 mA cm^{-2} from the start to 72 h into the experiment. Measurements of the concentration of dissolved In ions in the electrolyte indicated negligible dissolution (<0.2 nm) of InP over the 72-h CA (Figure 4c).

Due to the unchanged J-E behavior, the CA test of the p-InP/Pt was stopped after 72 h for further surface analysis. SEM images showed that discrete Pt particles remained on the p-InP surface after the CA (Figure 4d). The atomic-force microscopy (AFM) image in the region of the p-InP that had been directly exposed to the 1.0 M KOH(aq) electrolyte showed aggregated nanoparticles, with a surface roughness (R_q) of 1.7 nm (Figure S17). The XPS data of the p-InP/Pt electrode for the In 3d region (Figure 4e) displayed a distinct peak at higher BE = 444.8 eV ascribable to InO_x,[33–35] in addition to the peak at lower BE = 444.2 eV assigned to the In^{3+} cations of InP. Consistently, the XPS data in the O 1s region displayed a pronounced peak at 529.9 eV attributable to InO_x (Figure S18).[29,36,37] The XPS data in the P 2p region showed peaks at BEs <130 eV that are ascribable to the P^{3-} anions in InP, as well as a small peak at BE ~132 eV indicative of PO_x (Figure 4f). Notably, the increased atomic ratio of In/P (~3.1) after 72 h of operation indicated a substantial enrichment of In at electrode surface. Such In enrichment was not observed for the same p-InP/Pt electrode that underwent only 3 cycles of CV in 1.0 M KOH(aq), whose surface In/P ratio remained at ~1.3 (Figure S19-20).

Cross-sectional TEM images were obtained for a p-InP/Pt electrode after 72 h of CA in 1.0 M KOH (aq) (Figure 5a-c). A conformal overlayer attributable to the InO_x observed in the XPS data was evident on the exposed InP surface (Figure 5a). A higher magnification TEM image of the InP/InO_x interface revealed that this overlayer was amorphous and had a maximum thickness of 7 nm (Figure 5b). This amorphous layer was not observed at the InP/Pt interface (Figure 5c). An

energy-dispersive X-ray spectroscopy (EDS) line scan showed that the atomic fraction of P gradually decreased from 50% to 0% within the 5 nm region beyond InP (In/P~1), accompanied by a rapid increase in the number of O atoms (Figure 5d). Collectively, these data suggest a gradient InP/$InPO_x$/InO_x interfacial region, consistent with the XPS analyses. The EDS mapping also confirmed the enrichment of In and O relative to P in the region beyond InP. Pt and Fe (~20 at.%) were observed in addition to the amorphous $InPO_x$/InO_x layer. The Pt was located closer to the InP substrate than Fe, implying that these small Pt particles resulted from the prior electrodeposition. Consistent with the EDS mapping, the XPS of Fe 2p (Figure S21) revealed weak but observable signals attributable to trace FeO_x species (BE~711 eV), which may have been incorporated into the surface oxide from the 1.0 M KOH(aq) electrolyte during the long-term CA.[38,39]

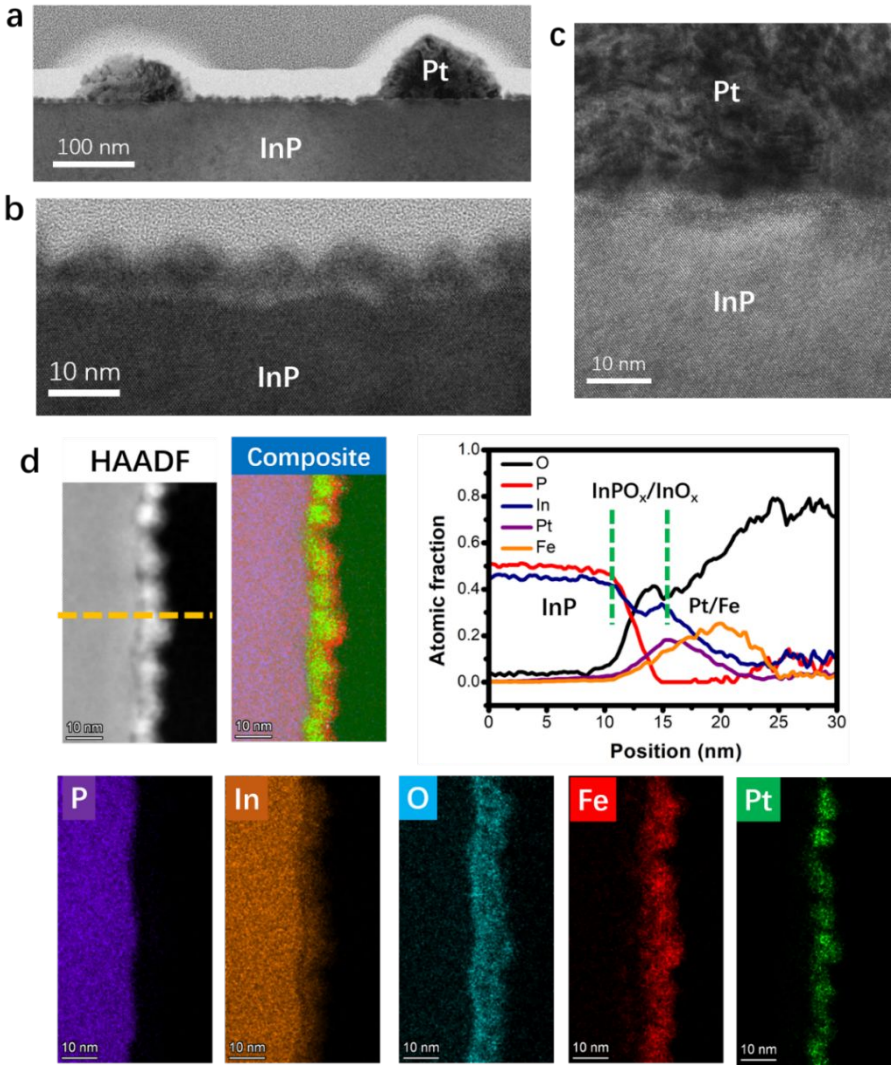

Figure 5. (a-c) Cross-sectional TEM images and (d) high-angle annular dark-field (HAADF) image, EDS maps and EDS line scan of the p-InP/Pt photoelectrode after 72 h at 0 V vs RHE in 1.0 M KOH(aq) under 1-sun illumination.

To robustly attribute the degradation in the *J-E* behavior to formation of interfacial InO_x, the illuminated p-InP/Pt electrode was first held in 1.0 M KOH(aq) at E = 0 V vs RHE for 15 h and was then immersed in 1.0 M H_2SO_4(aq). After the 15-h CA in 1.0 M KOH(aq), the *J-E* behavior shifted towards negative potentials, and E_{oc} decreased from 0.62 to 0.34 V vs RHE (Figure 6). However, when the degraded p-InP/Pt electrode was immersed in 1.0 M H_2SO_4(aq), the *J-E* behavior was immediately restored to its original shape before the CA, accompanied by an increase in E_{oc} to 0.66 V vs RHE. The XPS data (Figure S22) confirmed that after exposure to 1.0 M H_2SO_4(aq), the electrode surface was restored to nearly stoichiometric InP (In/P=1.2) and no peak ascribable to InO_x was observed in either the O 1s and In 3d XPS regions.

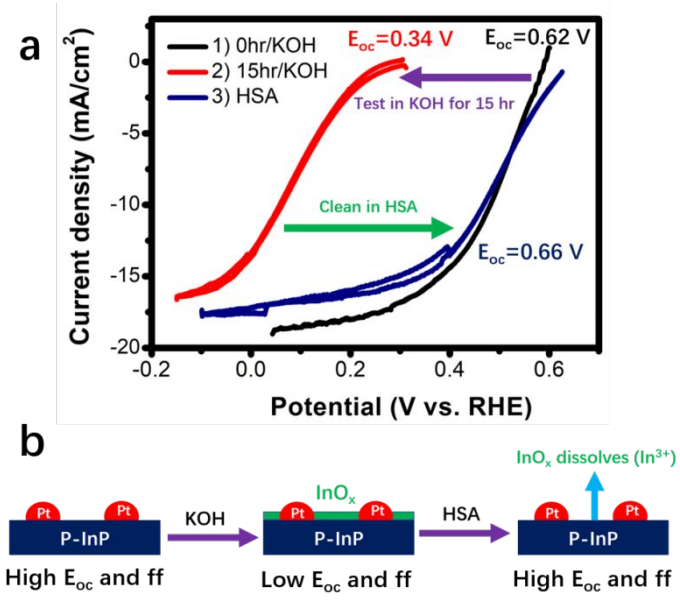

Figure 6. (a) Comparison of the *J-E* behavior of the illuminated p-InP/Pt electrode before (black) and after (red) testing at 0 V vs RHE for 15 h in 1.0 M KOH(aq) and then after (blue) exposure to 1.0 M H_2SO_4(aq). Scan rate: 50 mV s^{-1}. (b) Schematic illustration of the formation of InO_x on InP during the stability test in 1.0 M KOH(aq) and its subsequent dissolution in 1.0 M H_2SO_4(aq). V_{oc} and *ff* represent the open-circuit voltage and fill factor of the photoelectrode, respectively.

The XPS analyses of p-InP/Pt at pH 0 and pH 14 indicate that under both conditions the presence of Pt inhibited the cathodic corrosion of p-InP to form metallic In^0. To further understand the kinetic effect of the Pt HER catalyst, the stability of n-InP and n-InP/Pt electrodes was evaluated in the dark at E = -0.1 V vs RHE in 1.0 M H_2SO_4(aq) or 1.0 M KOH(aq) (Figure S23-24). The value of E = -0.1 V vs RHE matched the overpotential of a Pt catalyst when producing J=-10 mA cm^{-2} for the HER.[40] Use of n-InP electrodes, in which electrons are majority charge carriers, in the dark allows deconvolution of photovoltage effects that are inherent in illuminated p-InP electrodes. A dissolution rate of ~0.3 nm h^{-1} was observed for an etched n-InP electrode evaluated for 72 h in 1.0 M H_2SO_4(aq) at E = -0.1 V vs RHE (Figure S23). After the CA in H_2SO_4, three independent etched n-InP electrodes, as well as an n-InP/Pt electrode, consistently displayed stoichiometric InP surfaces (In/P=1.2) with no appreciable additional species such as In^0 or PO_x (Figure S25 and S27). In 1.0 M KOH(aq), dissolution of In ions was not observed for either n-InP or n-InP/Pt electrodes (Figure S23-24). Two n-InP samples evaluated in KOH for different durations of CA showed a slight enrichment (In/P=1.4) in In, in the form of $In(OH)_3$, at the electrode surface (Figure S26). In contrast, the n-InP/Pt electrode displayed a stoichiometric InP surface after the CA in KOH (Figure S27). Compared to previous results in which n-InP electrodes were evaluated with CA at much more negative E than those used herein, metallic In^0 was not detected for any n-InP electrodes operated at E = -0.1 V vs RHE. These results indicate that the dissolution and surface conditions of illuminated p-InP/Pt electrodes resemble those of both n-InP and n-InP/Pt evaluated at E = -0.1 V vs RHE in the dark, at both pH 0 and pH 14.

Discussion

Pourbaix diagrams[10] that represent thermodynamic electrochemical equilibria in aqueous solutions are useful for analysis of the corrosion pathways of semiconducting materials. Although Pourbaix diagrams typically only consider ions and compounds formed between single elements and water, simultaneous consideration of the diagrams for each element in a compound provides insight into the reactions that can occur under various conditions of pH and E. Figure S28 shows a combined In-P Pourbaix diagram obtained from the Materials Project.[13] The formal oxidation states in InP are In^{3+}

and P^{3-}. The reaction of either element with water is irreversible, as InP is not predicted to be stable in any *E*-pH region. Table S1 shows the half-reactions of In and P relevant to the decomposition of InP at pH 0 and pH 14. Tables S2-3 summarize the experimental results obtained herein.

Cathodic corrosion of InP: At sufficiently negative *E*, electrochemical reduction of InP to metallic In^0 can occur, with the production of PH_3(g) at both pH = 0 and pH = 14 (Eq 3a-b):[25,26]

In acid: $$\mathrm{InP(s) + 3H^+(aq) + 3e^- \longrightarrow In(s) + PH_3}(g) \quad (3a)$$

In base: $$\mathrm{InP(s) + 3e^- + 3H_2O(l) \longrightarrow In(s) + PH_3(g) + 3OH^-}(aq) \quad (3b)$$

For Eq 3a, the formation energies of the species predict an InP/In^0 standard potential, E(InP/In^0), of ~-0.31 V vs RHE, close to the standard redox potential of the In^{3+}/In^0 couple (-0.34 V vs RHE at pH = 0). Eq 3a and 3b contain mutually the same number of protons/water and electrons, suggesting that as the pH is varied E(InP/In^0) should stay fixed relative to the RHE potential. Therefore, at pH = 14, E(InP/In^0) is predicted to be more negative than either E(In_2O_3/In^0) = -0.19 V vs RHE or E($In(OH)_3$/In^0) = -0.172 V vs RHE. In the dark, we observed appreciable In^0 plating on the n-InP surface at $E \leq$ -0.6 V vs RHE for pH 0 and at $E \leq$ -0.4 V vs RHE for pH 14, respectively. These results are consistent with the calculated value of E(InP/In^0).

Mott-Schottky analysis was performed at both pH 0 and pH 14 to estimate the band-edge positions of InP relative to the RHE (Figure S29a-d). For n-InP, the flat-band potentials (E_{fb}) were -0.34 V vs RHE in 1.0 M H_2SO_4(aq) and -0.27 V vs RHE in 1.0 M KOH(aq), whereas for p-InP, E_{fb} was 0.91 V vs RHE in 1.0 M H_2SO_4(aq) and was 0.95 V vs RHE in 1.0 M KOH(aq). E_{fb} of both n-InP and p-InP thus remained essentially constant relative to the RHE potential at pH 0 and 14. Figure S29e shows an analysis of the interfacial energetics between the band-edge positions of InP, the value of E(InP/In^0) and the RHE potential, which applies to both pH 0 and pH 14.[31,32]

The In^0 stripping waves shifted substantially (>0.4 V) between dark n-InP electrodes and illuminated p-InP photoelectrodes. As shown in Scheme 1a, the positive shifts are consistent with the expected photovoltage effect produced by the p-InP photoelectrode, leading to a splitting between the potentials of the quasi-Fermi levels (E_{qf}) of minority carriers (electrons) and majority carriers (holes). Under negative bias, the surface potential (E_{surf}) is expected to be much more negative than

the potential applied to the back contact of the electrode (E_{app}). Moreover, substantial In^0 plating was observed at the surface of illuminated p-InP electrodes when $E \leq +0.2$ V vs RHE for both pH = 0 and pH 14. Despite $E_{app} > E(InP/In^0)$, the occurrence of cathodic corrosion at the surface of the illuminated p-InP electrode suggests that the photogenerated electrons from the conduction band of p-InP are energetically able to promote the reduction of InP to In^0 at the InP/electrolyte interface.

The cathodic photocorrosion of p-InP to In^0 comprises a primary failure mode for the p-InP photocathode. The appearance of In^0 on the p-InP surface correlated with a rapid decay in cathodic $|J|$ at negative potentials. The decrease in $|J|$ is likely due to metallic In^0 being optically opaque with a high overpotential for the HER (Figure S30). Under negative bias, the plated In^0 metal on the InP surface was partially soluble at pH = 0 but almost insoluble at pH = 14. The cathodic corrosion of InP to In^0 can occur due to the slow kinetics of the HER at etched InP surfaces, resulting in a large overpotential (η) to effect $J > 10$ mA cm^{-2}. In the dark, an etched n-InP electrode produced $J = -1$ mA cm^{-2} at $E = -0.78$ V vs RHE in 1.0 M H_2SO_4(aq) and at $E = -0.66$ V vs RHE in 1.0 M KOH(aq), with both of these potentials much more negative than either $E(InP/In^0)$ or the RHE potential (Figure S31). As a consequence, under negative bias sufficient to produce cathodic currents through the InP, photogenerated electrons from illuminated etched p-InP electrodes compete between effecting the HER and the reduction of InP to In^0.

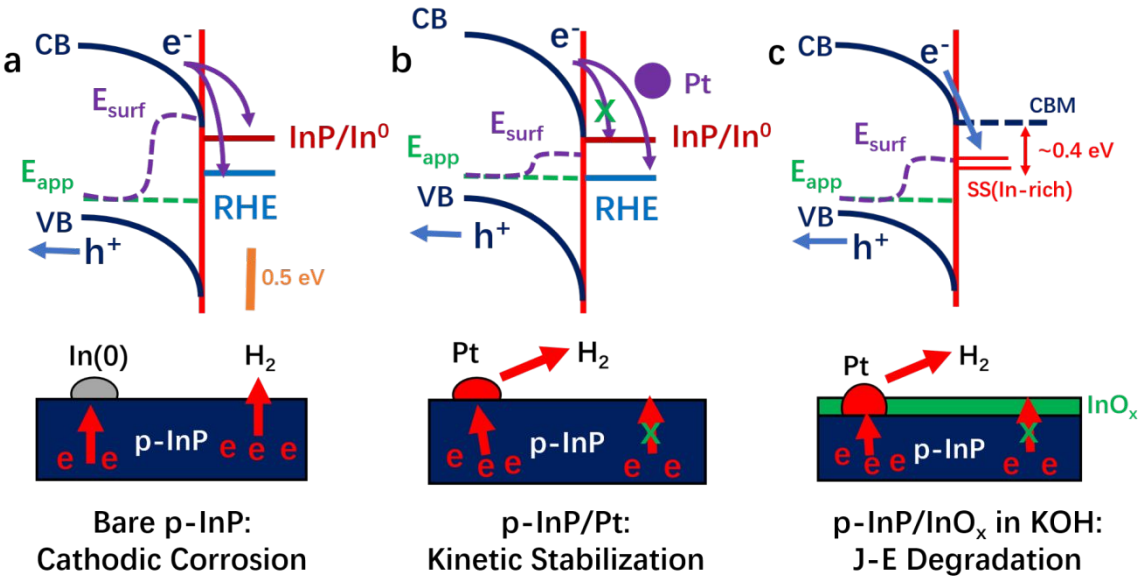

Scheme 1. Comparison of the band energy diagram and the direction of photogenerated electron (e^-) flow for (a) an etched p-InP electrode, (b) a p-InP/Pt electrode and (c) a p-InP/InO_x/Pt electrode under illumination in contact with 1.0 M KOH(aq). E_{app} and E_{surf} represent the applied potential at the back contact and the surface potential of photogenerated minority carriers (e^-), respectively. SS represents the surface states produced by an In-rich surface of p-InP, ~0.4 eV below the conduction-band minimum (CBM).[41] The horizontal lines marked InP/In^0 and RHE represent the thermodynamic equilibrium potentials for the cathodic corrosion of p-InP and for the HER, respectively, which are ~ -0.31 V vs RHE and 0 V vs RHE at both pH 0 and pH 14.

Kinetic stabilization of p-InP by the Pt catalyst: Metallic In^0 was not detected by XPS on illuminated p-InP/Pt electrodes after extended periods of CA at 0 V vs RHE at either pH 0 or pH 14 (Figure 3e and Figure 4e). These results suggest that the presence of Pt at p-InP surface inhibits cathodic corrosion. However, Pt only covers a fraction of the surface, leaving a large fraction of the p-InP surface exposed to the acidic or alkaline electrolyte. Because E(InP/In^0) is more negative than the RHE, the HER is thermodynamically favored compared with the cathodic corrosion of InP. Hence, the lack of metallic In^0 formation reveals a kinetic effect of the Pt HER catalyst, consistent with expectations for Pt substantially reducing the kinetic η of the HER at the electrode surface. Based on the HER activity of Pt, a small η of < 200 mV is required to produce J = -20 mA cm^{-2}.[40,42] Under light-limited current densities (J_{ph}) for p-InP, the E_{surf} of p-InP/Pt occurs in a potential region between the RHE potential and E(InP/In^0), due to the facilitated surface kinetics (**Scheme 1b**). The spacing between electrodeposited Pt particles is within hundreds of nm, so the photogenerated electrons can be effectively collected at the Pt catalyst due to the large (typically a few microns) minority-carrier diffusion length of highly efficient p-InP samples.[43–45] Consequently, the photogenerated electrons from the p-InP can selectively perform the HER at the catalytic Pt sites under these photocurrent densities, without effecting the self-reduction of InP. The catalytic current densities at the Pt depend on the ratio of electrochemically active area of the Pt catalyst particles relative to the geometric area of the InP light absorber that determines the overall photocurrent density. Previous studies using the dual working electrode (DWE) technique support the expectation that the E_{surf} of the semiconductor photoelectrode is largely determined by the surface kinetics, and becomes fixed by J_{ph} even at increasingly negative E_{app} values.[46–48] These results thus reveal that the specific energy level of E_{surf} and the surface kinetics are important for defining the corrosion

chemistry of p-InP photoelectrodes, in accord with expectations based on early theories of semiconductor stability.[49,50]

As a result, the reaction pathways of the p-InP/Pt electrodes under the HER operation can be determined by referring to E = -0.1 V vs RHE in the In-P Pourbaix diagram at both pH 0 and pH 14:[51]

In acid: $InP(s) + 4H_2O(l) + 3H^+(aq) \longrightarrow In^{3+}(aq) + H_3PO_4(aq) + 4H_2(g)$ (4a)

In base: $2InP(s) + 6OH^-(aq) + 5H_2O(l) \longrightarrow In_2O_3(s) + 2PO_4^{-3}(aq) + 8H_2(g)$ (4b)

Insoluble In_2O_3 rather than dissolved InO_2^- ions is postulated for reaction 4b, due to the experimental observation that negligible dissolution of In ions was present at pH 14. Under illumination at both pH conditions, the potential of the Fermi level (E_f) of electrons or the surface potentials ($E_{f,n}$) are not sufficient energetically to effect the self-reduction of In^{3+} cations in InP. Thus, the main driving force for the corrosion of InP is the reduction of water or protons by the oxidation of the P^{3-} in InP. The reduction potentials of P(III) species to PH_3(g) (H_3PO_3 at pH 0 and HPO_3^{2-} at pH 14) are ~ -0.28 V vs RHE and ~ -0.48 V vs RHE at pH 0 and pH 14, respectively (Table S1). The observation that $E(P^{3+}/P^{3-})$ is negative relative to the RHE potential corroborates the hypothesis that the P^{3-} anions in InP have sufficient reducing power to reduce water or protons to H_2.

XPS analyses and ICP-MS measurements both support the proposed corrosion pathways (Eq 4a-b). In acidic electrolyte, the illuminated p-InP/Pt electrode displayed a dissolution rate of ~0.15 nm h^{-1} for the first 50 h, which slowed to ~0.03 nm h^{-1} after 150 h. The XPS data also show that during the CA at 0 V vs RHE, the p-InP/Pt surface remained nearly stoichiometric (In/P=1.2) in the first 25 h, corresponding to a stoichiometric dissolution of In and P into the electrolyte based on Eq 4a. Despite the predicted thermodynamic instability, the dissolution kinetics of illuminated the p-InP/Pt electrodes is sufficiently slow to provide an operationally stable photocathode for >285 h. The decreased dissolution rate after long-term operation of the HER (>150 h) is attributable to passivation of the surface with a PO_x/P^0 layer, resulting in a P-rich surface of p-InP. Under alkaline conditions, the p-InP/Pt electrode evaluated by CA at 0 V vs RHE exhibited negligible dissolution over 72 h. However, the surface of p-InP was enriched with InO_x, indicating a surface conversion

process (Eq 2b). The preserved InO_x layer at the p-InP surface after the 72-h CA at 0 V vs RHE also suggests a much lower solubility of InO_x in 1.0 M KOH(aq) than in 1.0 M H_2SO_4(aq), resulting in different surface conditions at different pH values of of electrolyte.

pH-dependent evolution of the *J-E* behavior: The long-term evolution of the *J-E* behavior of illuminated p-InP/Pt electrodes also depends on the pH of the electrolyte. In acidic electrolytes, the *J-E* behavior remained nearly unchanged for as long as 285 h, despite the slightly lower E_{oc}. This behavior was accompanied by: (1) a nearly stoichiometric InP surface in the initial 25 h of CA, which then converted into a P-rich surface; and (2) a slow but continuous leaching of In^{3+} ions from electrode surface. In contrast, continuous leaching of In ions was not observed for the illuminated p-InP/Pt electrode in 1.0 M KOH(aq). Instead, the surface passivation of p-InP with InO_x caused substantial degradation in the *J-E* behavior of a p-InP/Pt electrode. These results reveal the importance of surface stoichiometry (In/P atomic ratio) for determining the long-term evolution of the *J-E* behavior of p-InP/Pt photocathodes.

Based on the unified defect model proposed by Spicer and co-workers, a non-stoichiometric surface of InP with additional In or P atoms can lead to surface states (SS) within the band gap, altering the electrical behavior of the interface.[41,52,53] According to this model, an In-rich surface and a P-rich surface of InP create surface states located 0.4 eV and 0.1 eV below the conduction-band minimum (CBM), respectively. Thus, for p-InP, the impact of Fermi level pinning by SS is expected to be more pronounced for an In-rich surface (Scheme 1c). The evolution in the *J-E* behavior of illuminated p-InP/Pt electrodes reported herein is consistent with this model. After long-term CAs, the In-rich surface of p-InP that formed in alkaline electrolytes caused a more substantial degradation of the *J-E* behavior of p-InP/Pt electrodes than was observed for surfaces operated electrochemically in acidic electrolytes.

These results moreover suggest that the physical stability (dissolution) and electrochemical stability (decay in *J*) of a p-InP/Pt electrode need to be considered separately. At pH = 0, the p-InP/Pt photoelectrode is physically unstable and exhibits a slow rate of dissolution, while providing stable PEC performance. At pH = 14, the p-InP/Pt photoelectrode remains physically robust without continuous dissolution, but the PEC performance degrades over time.

As shown in the In-P Pourbaix diagram (Figure S27), InP is not predicted to be a stable phase in any *E*-pH region, indicating its thermodynamic tendency to undergo surface corrosion via In-P dissociation in an aqueous environment. A comparison between the different changes in surface conditions of p-InP/Pt at pH = 0 and pH 14 suggests that the formation of InO_x at the surface of p-InP/Pt may be universal regardless of pH. However, the higher solubility of InO_x in acidic electrolytes allowed the dissolution of the InO_x upon formation, whereas in alkaline electrolytes the InO_x is insoluble and led to surface passivation. The stable PEC performance of p-InP/Pt at pH 0 is thus ascribable to a "self-cleaning" behavior that maintains a nearly stoichiometric surface by slowly dissolving the detrimental InO_x layer and leaching out In^{3+} ions. This hypothesis is further supported by the immediate recovery of the *J-E* behavior of the KOH-degraded p-InP/Pt electrode after exposure to acidic electrolytes. Further strategies for the development of stable p-InP photocathodes in either acidic or alkaline electrolytes could consequently focus on minimization of continuous dissolution while preserving a stoichiometric surface to enable stable PEC performance.

Outlook: The present work has implications that can be generalized for understanding the stability and corrosion mechanism of semiconductor photoelectrodes. The photovoltage produced by the semiconductor may complicate a direct analysis of the thermodynamic potentials of corrosion reactions. Hence, this photovoltage effect needs to be deconvoluted from the surface thermodynamic potentials to understand the fundamentals of the corrosion chemistry at the front-surface of the photoelectrode. Due to varied overpotentials at a given *J*, the catalytic kinetics at the electrode surface are crucial for defining the corrosion pathways at semiconductor/electrolyte interfaces, based on the Pourbaix diagram. For the HER, the presence of electrocatalysts such as Pt moves the surface potential closer to the RHE potential, which may result in a different corrosion chemistry than is present at an etched semiconductor surface. The onset potentials for the corrosion reactions should moreover be compared to the potentials for the fuel-forming reactions to identify a possible stability window that would take advantage of both thermodynamics and kinetics. For p-InP, cathodic corrosion can be systematically inhibited by accelerating the surface kinetics of the thermodynamically favored HER. Furthermore, the *J-E* behavior of the semiconductor photoelectrode is sensitive to the changes in surface stoichiometry, and a non-stoichiometric surface

can lead to operational instability. Thus, the physical stability and electrochemical stability of semiconductor photoelectrodes need to considered separately. Overall, this work provides insights into rationally understanding the stability of semiconductor photoelectrodes and consequently is beneficial for designing further strategies towards the realization of stable solar fuel devices.

Conclusions

The stability of p-InP has been evaluated for use as a photocathode for the HER in both 1.0 M H_2SO_4(aq) and 1.0 M KOH(aq), with or without an electrodeposited Pt catalyst. The corrosion mechanisms of etched p-InP and p-InP/Pt photoelectrodes were systematically established using XPS to monitor changes in the surface conditions after electrochemical tests, and the electrode dissolution over time was assessed using ICP-MS. In either 1.0 M H_2SO_4(aq) or 1.0 M KOH(aq), illuminated etched p-InP photoelectrodes underwent cathodic corrosion to form metallic In^0 at the electrode surface. In contrast, electrodeposited Pt at p-InP surfaces kinetically stabilizes illuminated p-InP electrodes against self-reduction in both 1.0 M H_2SO_4(aq) and 1.0 M KOH(aq). When held at E = 0 V vs RHE in acidic electrolytes, the p-InP/Pt photoelectrode exhibited a stable J of ~ -18 mA cm^{-2} for >285 h. The long-term evolution of the *J-E* behavior of the p-InP/Pt photoelectrode was dependent on the pH of the electrolyte, and strongly correlated with surface changes as well as with the dissolution of InP. In 1.0 M H_2SO_4(aq), the surface of p-InP/Pt electrode gradually turned P-rich with slow and continuous leaching of In ions, while the *J-E* behavior remained essentially unchanged. In 1.0 M KOH(aq), the p-InP/Pt electrode exhibited negligible dissolution while forming a passivating InO_x layer that caused substantial degradation in the *J-E* performance. This work reveals the importance of both catalytic kinetics and surface stoichiometry for defining the long-term stability of semiconductor photoelectrodes.

Acknowledgement

This material is based upon work performed by the Joint Center for Artificial Photosynthesis, a DOE Energy Innovation Hub, supported through the office of Science of the U.S. Department of Energy

under Award Number DE-SC0004993 and under award DE-SC0022087 from the Office of Basic Energy Sciences Office of the DOE. Research was in part carried out at the Molecular Materials Resource Center (MMRC) of the Beckman Institute of the California Institute of Technology. W. Yu and C. G. Read acknowledge the Resnick Sustainability Institute (RSI) at Caltech for fellowship support. I. A. Moreno-Hernandez acknowledges a National Science Foundation Graduate Research Fellowship (Grant No. DGE-1144469). Prof. Dr. Hans-Joachim Lewerenz, Dr. Ke Sun and Dr. Chengxiang Xiang are gratefully acknowledged for inspiring discussions. Dr. Kimberly M. Papadantonakis is thanked for assistance with manuscript editing. Dr. Nathan Dalleska is thanked for assistance with ICP-MS analyses. Ryan Jones is acknowledged for assistance with the design of the compression cell. Sean Byrne and Heng Dong are acknowledged for assistance with experiments.

References

1 O. Khaselev and J. A. Turner, *Science*, 1998, **280**, 425.
2 S. Tembhurne, F. Nandjou and S. Haussener, *Nat Energy*, 2019, **4**, 399–407.
3 W.-H. Cheng, M. H. Richter, M. M. May, J. Ohlmann, D. Lackner, F. Dimroth, T. Hannappel, H. A. Atwater and H.-J. Lewerenz, *ACS Energy Letters*, 2018, **3**, 1795–1800.
4 S. Licht, *International Journal of Hydrogen Energy*, 2001, **26**, 653–659.
5 M. M. May, H.-J. Lewerenz, D. Lackner, F. Dimroth and T. Hannappel, *Nature Communications*, 2015, **6**, 8286.
6 M. Ben-Naim, R. J. Britto, C. W. Aldridge, R. Mow, M. A. Steiner, A. C. Nielander, L. A. King, D. J. Friedman, T. G. Deutsch, J. L. Young and T. F. Jaramillo, *ACS Energy Letters*, 2020, **5**, 2631–2640.
7 M. R. Singh, K. Papadantonakis, C. Xiang and N. S. Lewis, *Energy & Environmental Science*, 2015, **8**, 2760–2767.
8 J. Jin, K. Walczak, M. R. Singh, C. Karp, N. S. Lewis and C. Xiang, *Energy Environ. Sci.*, 2014, **7**, 3371–3380.
9 S. Hu, C. Xiang, S. Haussener, A. D. Berger and N. S. Lewis, *Energy & Environmental Science*, 2013, **6**, 2984–2993.
10 M. Pourbaix, *Atlas of electrochemical equilibria in aqueous solutions*.
11 S. Chen and L.-W. Wang, *Chemistry of Materials*, 2012, **24**, 3659–3666.
12 A. Jain, S. P. Ong, G. Hautier, W. Chen, W. D. Richards, S. Dacek, S. Cholia, D. Gunter, D. Skinner, G. Ceder and K. A. Persson, *APL Materials*, 2013, **1**, 011002.
13 K. A. Persson, B. Waldwick, P. Lazic and G. Ceder, *Physical Review B*, , DOI:10.1103/PhysRevB.85.235438.
14 A. K. Singh, L. Zhou, A. Shinde, S. K. Suram, J. H. Montoya, D. Winston, J. M. Gregoire and K. A. Persson, *Chemistry of Materials*, 2017, **29**, 10159–10167.

15 J. F. Geisz, M. A. Steiner, N. Jain, K. L. Schulte, R. M. France, W. E. McMahon, E. E. Perl and D. J. Friedman, *IEEE J. Photovoltaics*, 2018, **8**, 626–632.
16 J. L. Young, M. A. Steiner, H. Döscher, R. M. France, J. A. Turner and T. G. Deutsch, *Nature Energy*, 2017, **2**, 17028.
17 E. Verlage, S. Hu, R. Liu, R. J. R. Jones, K. Sun, C. Xiang, N. S. Lewis and H. A. Atwater, *Energy & Environmental Science*, 2015, **8**, 3166–3172.
18 A. Heller and R. G. Vadimsky, *Physical Review Letters*, 1981, **46**, 1153–1156.
19 A. Heller, E. Aharon-Shalom, W. A. Bonner and B. Miller, *Journal of the American Chemical Society*, 1982, **104**, 6942–6948.
20 A. Heller, B. Miller, H. J. Lewerenz and K. J. Bachmann, *Journal of the American Chemical Society*, 1980, **102**, 6555–6556.
21 M. H. Lee, K. Takei, J. Zhang, R. Kapadia, M. Zheng, Y.-Z. Chen, J. Nah, T. S. Matthews, Y.-L. Chueh, J. W. Ager and A. Javey, *Angewandte Chemie*, 2012, **124**, 10918–10922.
22 M. Hettick, M. Zheng, Y. Lin, C. M. Sutter-Fella, J. W. Ager and A. Javey, *J Phys Chem Lett*, 2015, **6**, 2177–82.
23 Y. Lin, R. Kapadia, J. Yang, M. Zheng, K. Chen, M. Hettick, X. Yin, C. Battaglia, I. D. Sharp, J. W. Ager and A. Javey, *J. Phys. Chem. C*, 2015, **119**, 2308–2313.
24 L. Gao, Y. Cui, R. H. J. Vervuurt, D. van Dam, R. P. J. van Veldhoven, J. P. Hofmann, A. A. Bol, J. E. M. Haverkort, P. H. L. Notten, E. P. A. M. Bakkers and E. J. M. Hensen, *Advanced Functional Materials*, 2016, **26**, 679–686.
25 P. Bogdanoff, P. Friebe and N. Alonso-Vante, *J. Electrochem. Soc.*, 1998, **145**, 576–582.
26 A. Goryachev, L. Gao, R. P. J. van Veldhoven, J. E. M. Haverkort, J. P. Hofmann and E. J. M. Hensen, *Phys Chem Chem Phys*, 2018, **20**, 14242–14250.
27 A. Heller, B. Miller and F. A. Thiel, *Applied Physics Letters*, 1981, **38**, 282–284.
28 E. Aharon-Shalom and A. Heller, *Journal of The Electrochemical Society*, 1982, **129**, 2865–2866.
29 Z. M. Detweiler, S. M. Wulfsberg, M. G. Frith, A. B. Bocarsly and S. L. Bernasek, *Surface Science*, 2016, **648**, 188–195.
30 A. J. Bard, R. Parsons and J. Jordan, *Standard potentials in aqueous solution*, CRC press, 1985, vol. 6.
31 K. H. Schulte and H. J. Lewerenz, *Electrochimica Acta*, 2002, **47**, 2633–2638.
32 H. J. Lewerenz and K. H. Schulte, *Electrochimica Acta*, 2002, **47**, 2639–2651.
33 P. Kościelniak, J. Mazur, J. Henek, M. Kwoka, Ł. Pawela and J. Szuber, *Thin Solid Films*, 2011, **520**, 927–931.
34 R. Bayón, C. Maffiotte and J. Herrero, *Thin Solid Films*, 1999, **353**, 100–107.
35 T. Ishida, H. Kobayashi and Y. Nakato, *Journal of Applied Physics*, 1993, **73**, 4344–4350.
36 T. L. Barr and Ying Li Liu, *Journal of Physics and Chemistry of Solids*, 1989, **50**, 657–664.
37 J. L. White and A. B. Bocarsly, *J. Electrochem. Soc.*, 2016, **163**, H410–H416.
38 L. Trotochaud, S. L. Young, J. K. Ranney and S. W. Boettcher, *J Am Chem Soc*, 2014, **136**, 6744–53.
39 K. Sun, M. T. McDowell, A. C. Nielander, S. Hu, M. R. Shaner, F. Yang, B. S. Brunschwig and N. S. Lewis, *The Journal of Physical Chemistry Letters*, 2015, **6**, 592–598.

40 C. C. L. McCrory, S. Jung, I. M. Ferrer, S. M. Chatman, J. C. Peters and T. F. Jaramillo, *Journal of the American Chemical Society*, 2015, **137**, 4347–4357.
41 W. E. Spicer, I. Lindau, P. Skeath and C. Y. Su, *Journal of Vacuum Science and Technology*, 1980, **17**, 1019–1027.
42 F. H. Saadi, A. I. Carim, E. Verlage, J. C. Hemminger, N. S. Lewis and M. P. Soriaga, *The Journal of Physical Chemistry C*, 2014, **118**, 29294–29300.
43 H. J. Lewerenz, C. Heine, K. Skorupska, N. Szabo, T. Hannappel, T. Vo-Dinh, S. A. Campbell, H. W. Klemm and A. G. Muñoz, *Energy & Environmental Science*, 2010, **3**, 748.
44 A. Heller, *Science*, 1984, **223**, 1141–1148.
45 B. M. Kayes, H. A. Atwater and N. S. Lewis, *Journal of Applied Physics*, 2005, **97**, 114302.
46 F. A. L. Laskowski, M. R. Nellist, R. Venkatkarthick and S. W. Boettcher, *Energy & Environmental Science*, 2017, **10**, 570–579.
47 F. Lin and S. W. Boettcher, *Nat Mater*, 2014, **13**, 81–6.
48 M. R. Nellist, F. A. Laskowski, F. Lin, T. J. Mills and S. W. Boettcher, *Acc Chem Res*, 2016, **49**, 733–40.
49 H. Gerischer, *Journal of Vacuum Science and Technology*, 1978, **15**, 1422–1428.
50 A. J. Bard and M. S. Wrighton, *Journal of The Electrochemical Society*, 1977, **124**, 1706–1710.
51 M. M. May, H.-J. Lewerenz and T. Hannappel, *The Journal of Physical Chemistry C*, 2014, **118**, 19032–19041.
52 W. E. Spicer, *Journal of Vacuum Science & Technology B: Microelectronics and Nanometer Structures*, 1988, **6**, 1245.
53 W. E. Spicer, I. Lindau, P. Skeath, C. Y. Su and P. Chye, *Phys. Rev. Lett.*, 1980, **44**, 420–423.

Broader Context

Photoelectrochemical water splitting by semiconductor photoelectrodes offers a promising approach to convert solar energy into chemical fuels in one step. However, materials stability remains the most persistent challenge for developing operational and efficient integrated solar-driven water-splitting devices. Fundamentally understanding the corrosion mechanism of semiconductor electrodes under varied operational conditions underpins rational strategies to improve the device stability. In this work, by investigating the stability of p-InP photocathodes, we reveal the generalizable factors that control the photoelectrode stability. Specifically, illuminated etched p-InP photocathodes undergo cathodic corrosion to form metallic In^0 in both acidic and alkaline electrolytes. In contrast, electrodeposited Pt catalysts stabilize the p-InP surface against such cathodic corrosion *via* kinetic control. Furthermore, we observe that a non-stoichiometric surface of p-InP/Pt photocathode passivated by InO_x in KOH leads to a substantial degradation of the current density-potential (*J*-*E*) behavior over long term. Overall, both surface catalytic kinetics and surface stoichiometry are important considerations of evaluating the corrosion chemistry and long-term stability of semiconductor electrodes. This work also underscores the need to separately consider the physical stability (electrode dissolution) and electrochemical stability (*J*-*E* behavior) of solar fuels photoelectrodes.